Journal Name

ARTICLE TYPE

Cite this: DOI: 00.0000/xxxxxxxxxx

Emergence and stabilization of transient twisted defect structures in confined achiral liquid crystals at a phase transition. Supplemental materials

Jose X. Velez, Zhaofei Zheng, Daniel A. Beller and Francesca Serra

1 Supplemental videos

Here are the captions of the supplemental videos.

Supplemental video S1: transition from the twisted configuration to the escaped radial configuration in a capillary with square cross section filled with CCN-47.

Supplemental video S2: images taken at different planes showing two defect lines crossing each other in a square capillary filled with CCN-47.

Supplemental video S3: images taken at different planes showing two defect lines not crossing each other in a square capillary filled with CCN-47.

2 Supplemental information

2.1 Simulation description and parameters

For the numerical modeling we use the standard Landau-de Gennes Q-tensor approach with a finite difference scheme implemented on a regular cubic mesh. The free energy is the sum of the contribution of the Landau energy, the bulk elastic energy and the anchoring energy and it is calculated in the whole volume bounded by the capillary boundary surface. The defects are identified as the region where the order parameter S, the largest eigenvalue of the tensor, is significantly lower than the bulk order parameter S_0. In this system, the mesh size corresponds to the correlation length of the liquid crystals, roughly 4.5nm (Simulation Unit, SU). With this mesh size, the maximum total simulation size in this work corresponds to capillaries with radius around 112.5 nm and length around 675 nm.

The boundary conditions, the elastic constants and the anchoring constant are given as input. In the simulations presented in the paper, we use the two-constants approximation, where the splay and bend constant are equal K_1=$K_3 = 10^{-11}$N and the twist constant is lower and defined from the ratio K_2/K_3. However, here in SI we explore also other combinations of elastic constants, in particular the case when $K_1 = K_2 < K_3$. Once again K_2/K_3 is the relevant parameter. The capillary walls have homeotropic anchoring with strength corresponding to $W_h = 10^{-2}$ J m^{-2} (strong anchoring). There are no periodic boundary conditions at the end of the capillaries, but instead the ends of the capillary have very weak planar anchoring $W_p = 10^{-10}$ J m^{-2}, justified by the fact that the liquid crystal has an almost planar alignment in the cross section of the capillary. In the paper and in the supplemental materials, we refer to this value as weak degenerate planar anchoring, unless otherwise specified. We have verified that changing this anchoring by one order of magnitude (smaller or larger) does not affect the final configuration.

As parameter constants of the Landau energy A, B and C we used the typical values for 5CB, $A = -0.172 * 10^6$ J / m^3, $B = -2.12 * 10^6$ J/m^3, $C = +1.73 * 10^6$ J/m^3, which give a scalar order parameter around S_0=0.53 [1].

With three elastic constants, the total free energy density f is calculated as:

$$f = \frac{A}{2}tr(Q^2) + \frac{B}{3}tr(Q^3) + \frac{C}{4}(tr(Q^2))^2 + \frac{L_1}{2}\frac{\partial Q_{ij}}{\partial x_k}\frac{\partial Q_{ij}}{\partial x_k} + \frac{L_2}{2}\frac{\partial Q_{ij}}{\partial x_j}\frac{\partial Q_{ik}}{\partial x_k} + \frac{L_3}{2}Q_{ij}\frac{\partial Q_{kl}}{\partial x_j}\frac{\partial Q_{kl}}{\partial x_j}$$

where, in the uniaxial limit, the Q tensor has components $Q_{ab} = \frac{3}{2}S(n_a n_b - \frac{1}{3}\delta_a b)$, where n is the nematic director and S the scalar order parameter. The elastic constants L_1, L_2, L_3 are related to the elastic constants K_1, K_2 and K_3 by $L_1 = 2/(27S_0^2)(-K_1 + 3K_2 + K_3)$, $L_2 = 4/(27S_0^2)(K_1 - K_2)$ and $L_3 = 4/(27S_0^3)(K_3 - K_1)$.

With the two elastic constants approximation, the total free energy density f is calculated as:

$$f = \frac{A}{2}tr(Q^2) + \frac{B}{3}tr(Q^3) + \frac{C}{4}(tr(Q^2))^2 + \frac{L_1}{2}(\nabla \times Q)^2 + \frac{L_2}{2}(\nabla \cdot Q)^2$$

The two elastic constants L_1 and L_2 are related to the elastic constants K_1, K_2 and K_3 by $K_1 = K_3 = \frac{9}{4}S_0^2(L_1 + L_2)$ and $K_2 = \frac{9}{2}S_0^2 L_1$.

References

1 Ravnik, M., Zumer, S, *Liq. Crys.*, 36, 1201, 2009.

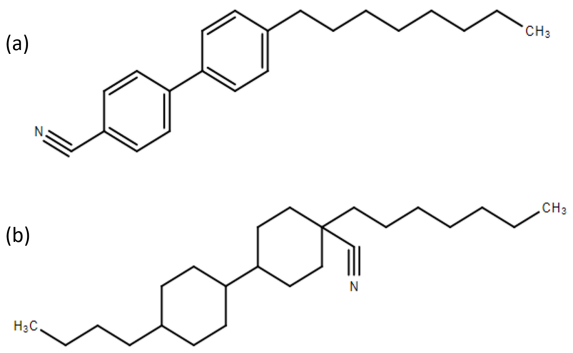

Fig. 1 Chemical structure of the liquid crystals 8CB (a) and CCN-47 (b).

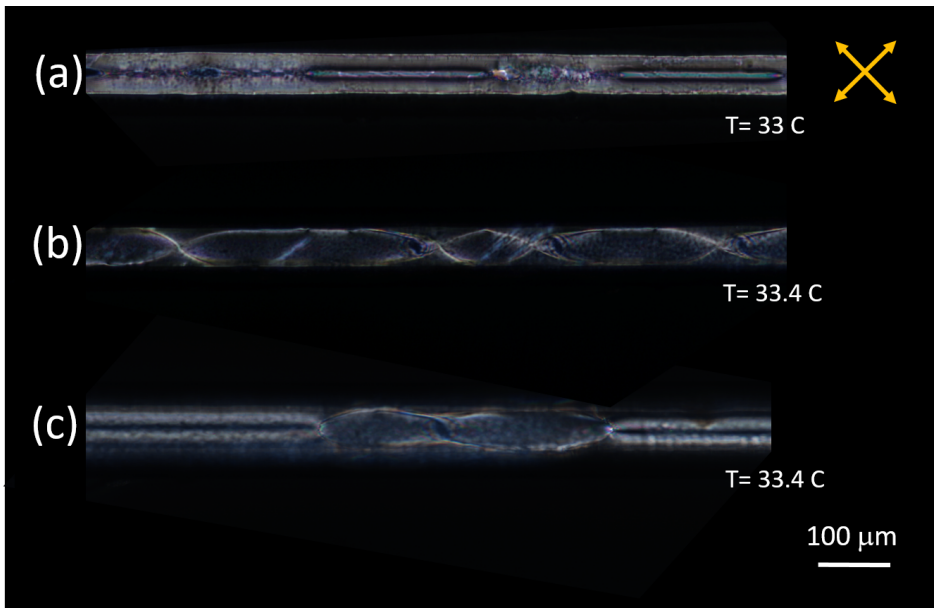

Fig. 2 Example of twisted configuration observed in a glass capillary with square cross section, with side 50μm, treated for homeotropic anchoring with octadecyl-trichlorosilane and filled with the common liquid crystal 8CB. The configuration is observed at the smectic-nematic phase transition; it is transient and unstable and eventually it is replaced by an escaped radial configuration. (a) Capillary at T=33^o C viewed under crossed polarizers, whose direction is indicated by the arrows; (b) the same capillary at T=33.4^o C; (c) capillary being held at the same temperature for about 5 minutes. It is possible to see how the escaped radial configuration takes over the twisted lines.

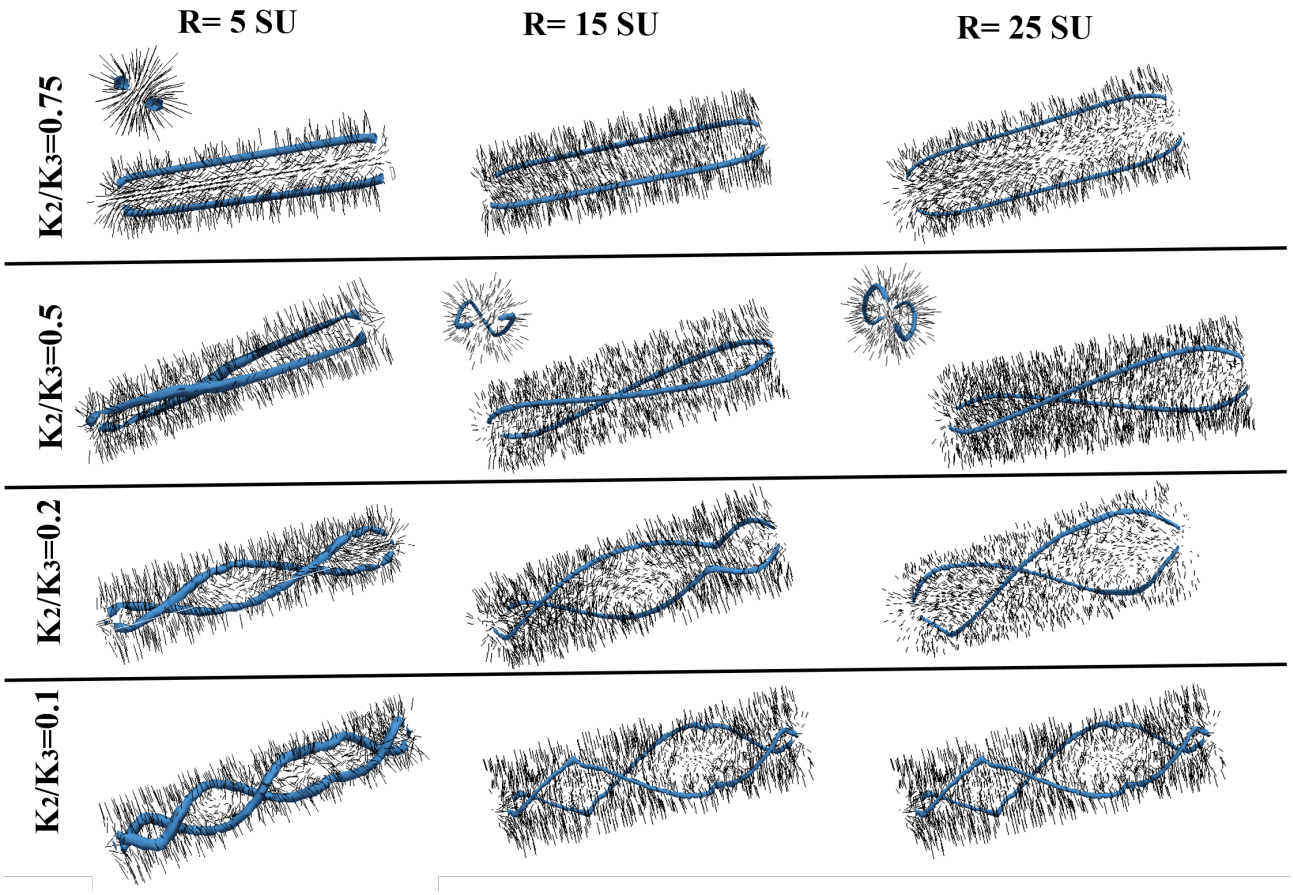

Fig. 3 Simulation of defects in capillaries with circular cross section with varying radii R and elastic anisotropy, for $K_1 = K_3$=10^{-11}N . The boundaries have strong homeotropic anchoring along the capillary walls and weak degenerate planar anchoring at the two ends (as explained in SI 2.1). The simulation unit is SU=4.5nm. In the insets we show the cross section (perpendicular to the capillary axis) for some configurations. For small elastic anisotropy K_2/K_3=0.75 the simulations show the Planar Polar achiral configuration. Twist arises for $K_2/K_3 \leq$0.5 for all radii tested. At low elastic anisotropy the defect helicity is smooth, but it progressively becomes more irregular as the anisotropy increases, at all radii. In the simulation, the length of the capillary varies, even though this does not affect the results. The lengths are 50, 100 and 150 SU respectively for the capillaries with radius 5, 15 and 25 SU.

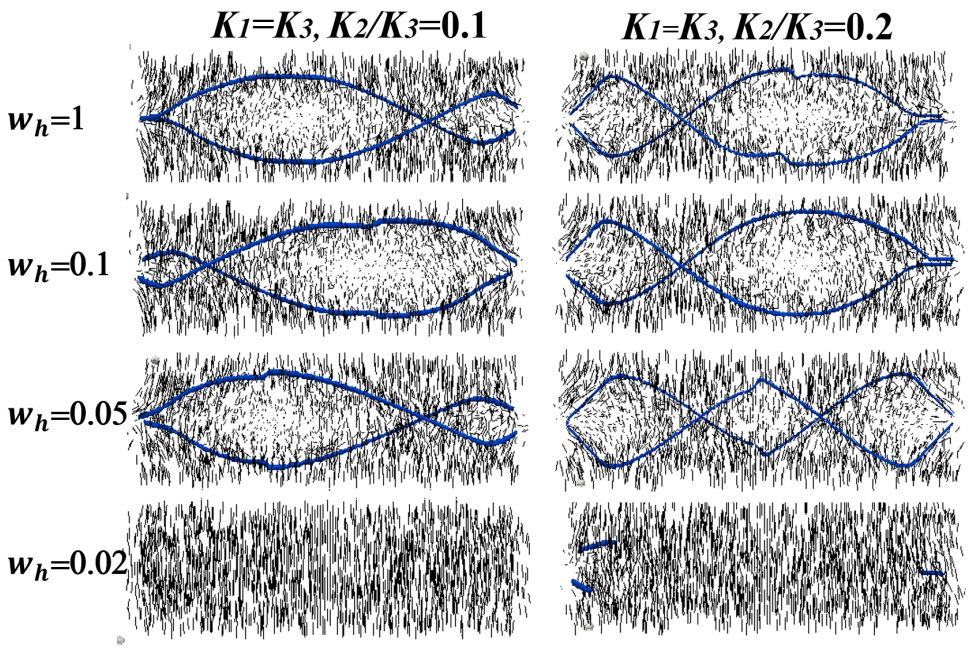

Fig. 4 Simulations of capillaries with circular cross section, radius 275nm (25 SU) and length 150 SU, with varying anchoring and elastic anisotropy, where $K_1 = K_3 > K_2$. Defects are highlighted in blue and the small glyphs indicate the nematic director. The anchoring at the two ends is very weak planar anchoring as specified in the SI section 2.1. Here, we vary the elastic anisotropy K_2/K_3 keeping K_3=10^{-11}N, and the anchoring constant. The parameter w_h describes the ratio between the anchoring constant used in the simulation and the strong homeotropic anchoring constant $W_h = 10^{-2}$ J m^{-2}. It is possible to see that for $w_h \geq 0.05$ the defects' helicity remains roughly the same and for lower w_h the system adopts a uniform planar configuration without defects, allowed by the weak anchoring.

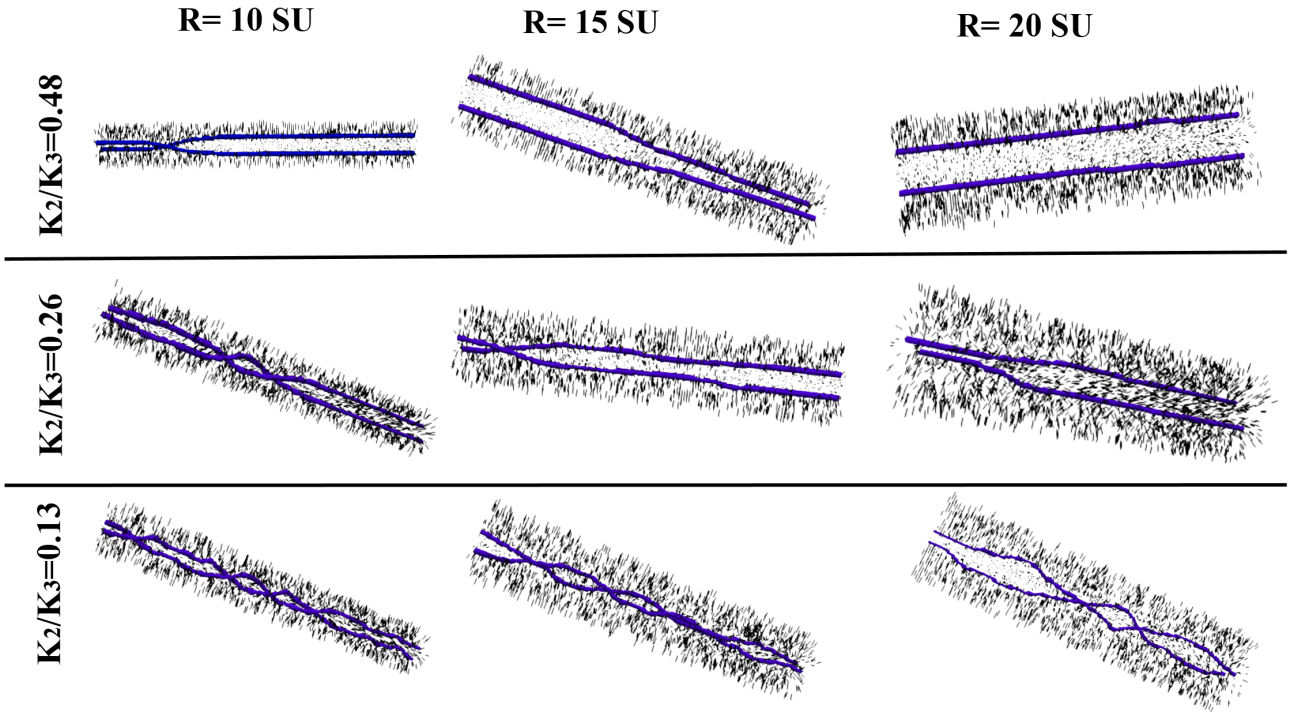

Fig. 5 Simulation of defects in capillaries with circular cross section with varying radii R (from 45 to 90nm) and elastic anisotropy, for $K_1 = K_2 < K_3$. The length of the capillary is 150 SU. The boundaries have strong homeotropic anchoring along the capillary walls and weak degenerate planar anchoring at the two ends, the elastic constants are for the three rows $K_2 = 2.4 * 10^{-12}$N, $K_2 = 1.6 * 10^{-12}$N and $K_2 = 10^{-12}$N respectively. The simulation unit is SU=4.5nm. The defects are highlighted in blue and the director field is shown by the black glyphs. For small elastic anisotropy K_3/K_2=2.1 the largest capillary shows the Planar Polar achiral configuration, while for smaller radii there is an onset of twist. Twist is evident for K_2/K_3=0.26 for all radii tested. At low elastic anisotropy twist is smooth, but it progressively becomes more irregular as the anisotropy increases, at all radii.

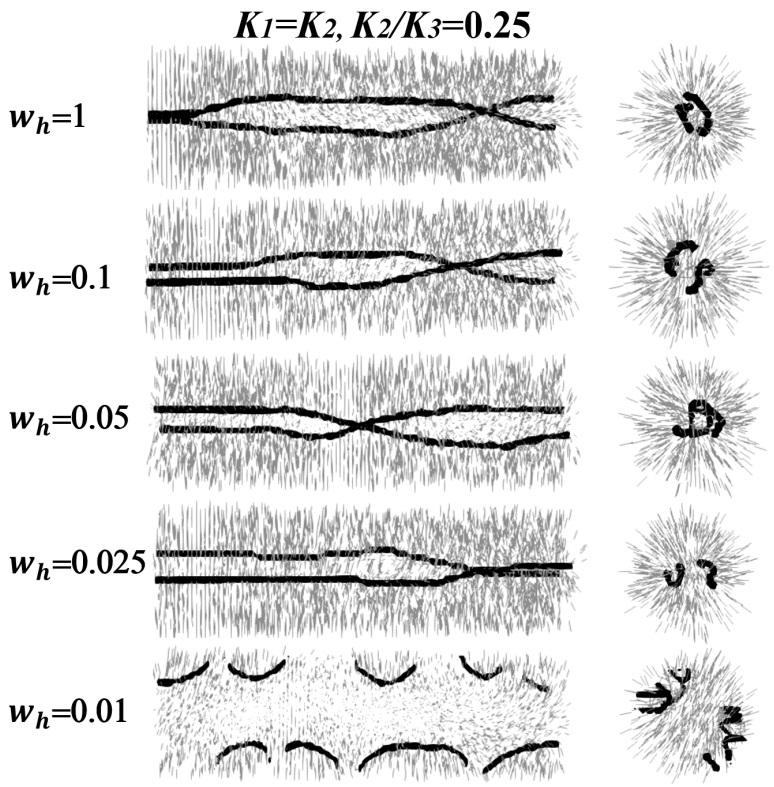

Fig. 6 Simulations of capillaries with circular cross section, diameter 135nm (30 SU) and length 100 SU, with varying anchoring and with K_1=K_2=2*10^{-12}N and K_3/K_2=4. Defects are highlighted in black and the small glyphs indicate the nematic director. The anchoring at the two ends of the capillary is very weak planar anchoring as specified in the SI section 2.1. Here, we vary the anchoring constant. The parameter w_h describes the ratio between the anchoring constant used in the simulation and the strong homeotropic anchoring constant $W_h = 10^{-2}$ J m^{-2}. It is possible to see that these simulations are even more robust than the ones shown in the previous figure, and that for $w_h \geq 0.025$ the defects' helicity remains roughly the same. For lower w_h the system the defect lines become irregular and the system tends to be uniform planar in the plane perpendicular to the capillary axis.

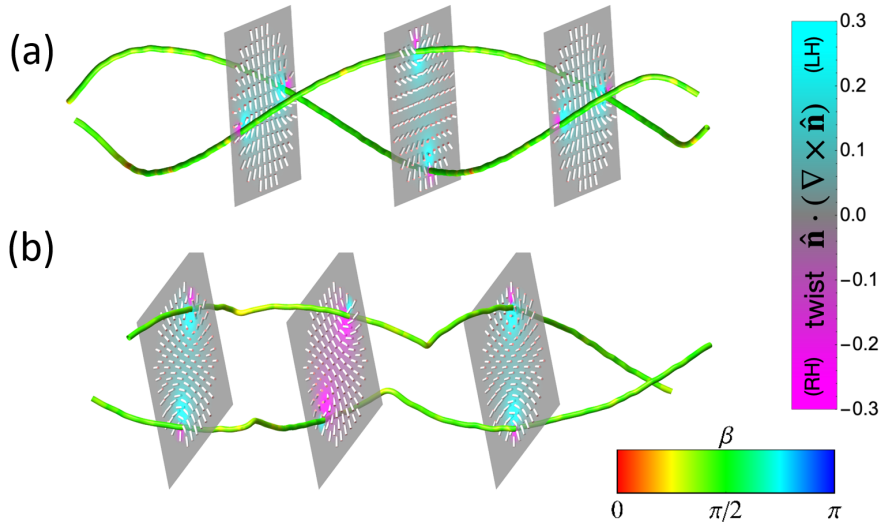

Fig. 7 Handedness of the twist around disclination lines. The simulations are the same as used in Fig. 2c (panel (a)) and 2e (panel (b)) in the main text. Here the twist is shown at various points along the lines, showing that the kinks are points of handedness inversion.

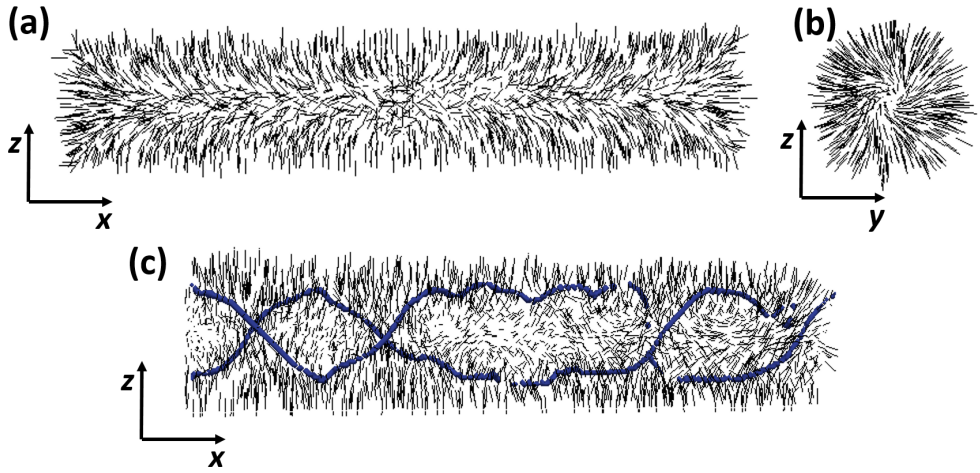

Fig. 8 Simulations of the twisted escape radial (TER) configurations, obtained as a metastable state by using an escaped radial configuration as initial state and introducing an elastic anisotropy with $K_1 = K_3 = 5K_2$. As in the other simulations in the paper, the system does not have periodic boundary conditions and the LC has weak planar anchoring on the two ends of the capillary. (a-b) Side view and view along the capillary diameter of the TER configuration. This defect-free state was obtained as a metastable configuration by increasing the value of the phase energy in the simulations by 2.6 times, which was done by modifying the values of A in the Landau energy, increasing it by five times. (c) Configuration obtained with the same phase energy relaxing the previous configuration and adding noise to escape the metastable state. The dark lines represent the twisted defects. The energy difference between the two configurations is 1100kT for a cylindrical capillary with 112.5 nm radius (25 SU) and 1125 nm length (2200 kT/μm^3) but it decreases to 140 kT/μm^3 for a capillary with 67.5 nm radius (15 SU).

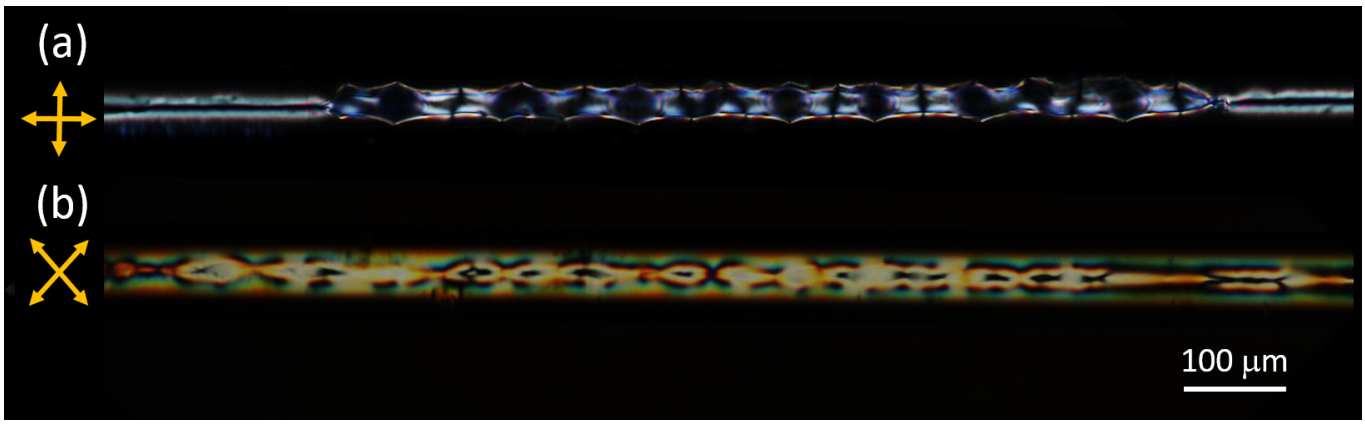

Fig. 9 Evidence of the lozenge pattern, as presented in figure 1 of the main text, in a glass capillary with circular cross section and 50 μm diameter. The configuration was observed at the smectic-nematic phase transition; however, it is extremely unstable and difficult to observe in capillaries with circular cross section. (a) Lozenge pattern forming in a capillary with round cross section treated with octadecyl-trichlorosilane and filled with 8CB. (b) Lozenge pattern forming in a capillary with round cross section filled with a mixture of CCN-47 and 0.1% of DDAB. The directions of the polarizers are indicated by the arrows.

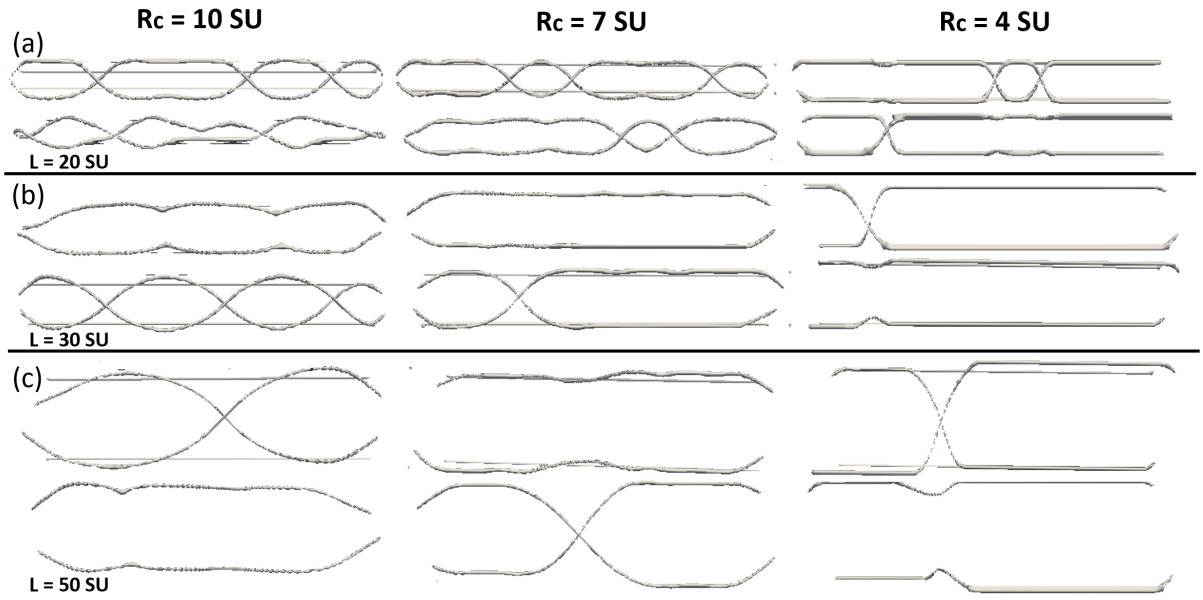

Fig. 10 Simulation of defects in capillaries with square cross section, with elastic constants $K_1 = K_3 > K_2$. The boundary conditions in these simulations are capillaries with square cross section and rounded corners. The length of the capillary is kept constant at 150 SU but the side of the square cross section L is varied from 20 SU (line (a)), to 30 SU (line (b)) and 50 SU (line (c)), corresponding to 90 nm-225 nm. The capillaries have radii of curvature of the corners R_c varying from 10 SU (rounded corners) to 4 SU (sharper corner). The boundaries have strong homeotropic anchoring along the capillary walls and weak planar anchoring at the two ends, the elastic constants are $K_1 = K_3$=10^{-11}N and $K_2 = 0.25K_3$. In every simulation, two different side views of the capillary are shown for clarity. In all cases, the defects form a smooth twist, or distorted twist configuration for larger radii of curvature, while they adopt the zig-zag configuration for the smallest radius of curvature. However, it is clear that in thinner capillaries the crossings of the capillary are more closely spaced.

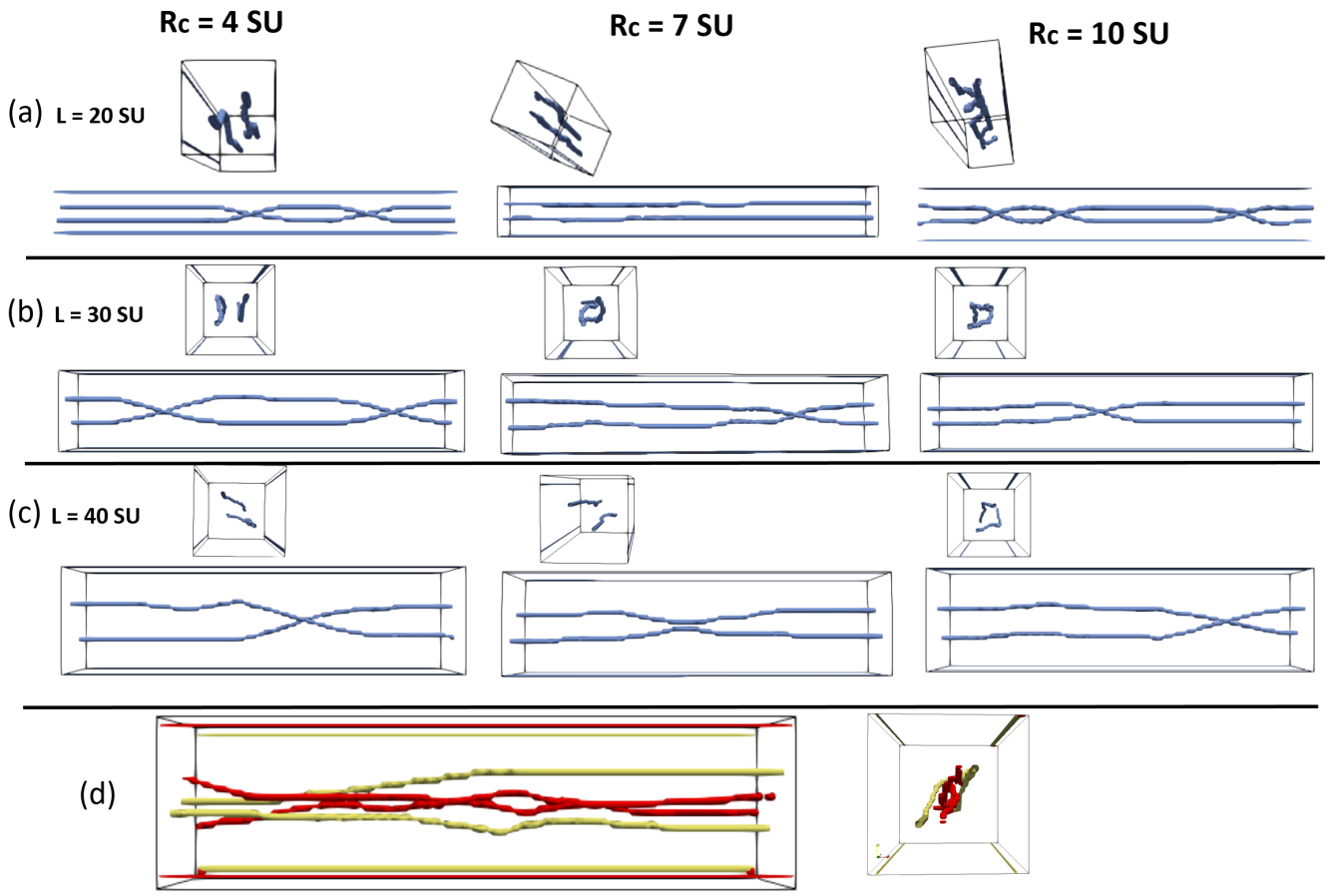

Fig. 11 Simulation of defects in capillaries with square cross section with elastic constants $K_1 = K_2 < K_3$. The boundary conditions in these simulations are capillaries with square cross section and rounded corners as in the previous figure. The length of the capillary is kept constant at 150 SU but the side of the square cross section L is varied from 20 SU (line (a)), to 30 SU (line (b)) and 40 SU (line (c)), corresponding to 90 nm-180 nm. The capillaries have radii of curvature of the corners R_c varying from 4 SU (sharp corners) to 10 SU (rounder corners). The boundaries have strong homeotropic anchoring along the capillary walls and weak random planar anchoring at the two ends, the elastic constants are $K_1 = K_2$=2*10^{-12} N and $K_3 = 4K_2$. In every simulation, the side view and the top view of the capillary are shown for clarity. In all cases, the regular twist is more difficult in the capillaries with sharper corners, which favor instead the zig-zag configuration where defect lines switch edges, as can be seen from the cross section. (d) Defect lines in a square capillary with smaller (red defects) and larger (yellow defects) value of K_1, while keeping K_2 and K_3 fixed. In the red curve, K_1 is reduced by a factor of 5. It is possible to see how decreasing K_1 leads to defect lines moving further away from the edges to the center of the capillary.

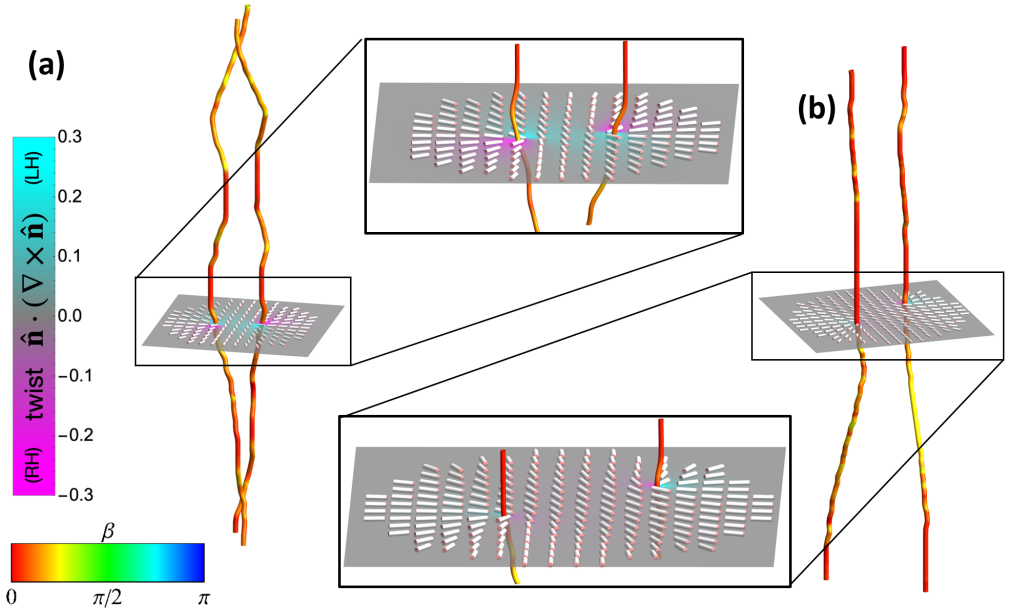

Fig. 12 Observation of twist and wedge characteristic of defect lines in capillaries with round and square cross section with elastic constants $K_1 = K_2 < K_3$. (a) Twist-wedge winding characteristic of the disclinations shown in Supplemental Figure 5, with $K_2/K_3 = 0.26$ and radius R=20 SU. (b) Twist-wedge winding characteristic of the disclinations shown in Supplemental Figure 11 with side equal to 40 SU and curvature radius of the edges equal to 4 SU. Insets show zoomed-in views of the director on one plane, with the plane colored by the local density of twist distortions.